The Astrophysical Journal, 973:146 (14pp), 2024 October 1 https://doi.org/10.3847/1538-4357/ad6844

Tracing the History of Obscured Star Formation with the SIMBA Cosmological Galaxy Evolution Simulation

Dhruv T. Zimmerman[1], Desika Narayanan[1,2,3], Katherine E. Whitaker[3,4], and Romeel Davé[5,6,7]

[1] Department of Astronomy, University of Florida, 211 Bryant Space Sciences Center, Gainesville, FL 32611, USA
[2] University of Florida Informatics Institute, 432 Newell Drive, CISE Bldg E251, Gainesville, FL 32611, USA
[3] Cosmic Dawn Center (DAWN), Niels Bohr Institute, University of Copenhagen, Jagtvej 128, København N, DK-2200, Denmark
[4] Department of Astronomy, University of Massachusetts Amherst, 710 N Pleasant Street, Amherst, MA 01003, USA
[5] SUPA, Institute for Astronomy, Royal Observatory, Blackford Hill, Edinburgh, EH9 3HJ, UK
[6] University of the Western Cape, Bellville, Cape Town 7535, South Africa
[7] South African Astronomical Observatories, Observatory Road, Cape Town 7925, South Africa

Received 2023 December 11; revised 2024 July 25; accepted 2024 July 25; published 2024 September 27

Abstract

We explore the cosmic evolution of the fraction of dust-obscured star formation predicted by the SIMBA cosmological hydrodynamic simulations featuring an on-the-fly model for dust formation, evolution, and destruction. We find that up to $z = 3$, our results are broadly consistent with previous observational results of little to no evolution in obscured star formation. However, at $z > 3$ we find strong evolution at fixed galaxy stellar mass toward greater amounts of obscured star formation, in tension with high-redshift observations. We explain the trend of increasing obscuration at higher redshifts by evolving star-dust geometry, as the dust-to-stellar mass ratios remain relatively constant across cosmic time. We additionally see that at a fixed redshift, more massive galaxies have a higher fraction of their star formation obscured, which is explained by increased dust-to-stellar mass ratios at higher stellar masses. Finally, we estimate the contribution of dust-obscured star formation to the total star formation rate budget and find that the dust-obscured star formation history peaks around $z \sim 2-3$, and becomes subdominant at $z \gtrsim 5$. The dominance of obscured star formation at redshifts $z \lesssim 4$ is consistent with our results for the evolution of the obscured star formation fraction at fixed stellar mass to higher values at higher redshift because there exist fewer massive, heavily obscured galaxies at high redshift.

Unified Astronomy Thesaurus concepts: Hydrodynamical simulations (767); Radiative transfer simulations (1967); Galaxy evolution (594); Dust physics (2229); Galaxy luminosities (603); Astrophysical dust processes (99); Interstellar dust extinction (837); Galaxy physics (612); Interstellar dust (836)

1. Introduction

Intimately tied with an understanding of the evolution of our Universe is the history of cosmic star formation. Star formation is responsible for many key processes that govern how galaxies evolve with time, such as depletion of galactic gas, stellar feedback into the interstellar medium (ISM), and chemical enrichment of the ISM for future generations of stars (see reviews such as Elmegreen & Scalo 2004; Scalo & Elmegreen 2004; Veilleux et al. 2005; Péroux & Howk 2020; Tacconi et al. 2020). Current observational constraints suggest that the majority of the star formation in the Universe took place during the epoch often referred to as "cosmic noon," at $z \sim 1-3$ (e.g., Madau & Dickinson 2014), though much of this star formation may be enshrouded in dust (Le Floc'h et al. 2009; Bouwens et al. 2016; Dunlop et al. 2017; Laporte et al. 2017; Bouwens et al. 2020; Casey et al. 2021). Therefore, in order to understand galaxy formation and evolution, we need also to understand the evolution in the amount of dust-obscured star formation at low and high redshift across the stellar mass function.

The current consensus from observations is that the relative amount of dust-obscured star formation at a fixed galaxy stellar mass does not strongly evolve with time up to $z \sim 3$ (e.g., Bouwens et al. 2016; Bourne et al. 2017; Whitaker et al. 2017; McLure et al. 2018) or roughly 85% of cosmic history. More recent higher-redshift observations suggest that galaxies beyond $z \gtrsim 4$ may have less of their star formation obscured (e.g., Fudamoto et al. 2020; Algera et al. 2023). Most of these results suggest that the main dependence of dust obscuration is on a galaxy's stellar mass; more massive galaxies are typically more obscured. Bouwens et al. (2016) and Whitaker et al. (2017) explore dust-obscured star formation by comparing the relative amount of light emitted from galaxies in samples stacked by stellar mass at the rest-frame ultraviolet (UV) and infrared (IR) wavelengths and see little redshift evolution. Bouwens et al. (2020) take advantage of the larger sample of higher-redshift galaxies available from Dudzevičiūtė et al. (2020) and find results for the stellar mass-obscured star formation relation consistent with their previous work in Bouwens et al. (2016). McLure et al. (2018) and Shapley et al. (2022) instead investigate dust attenuation curves up to $z \sim 3$ and similarly find minimal evolution in the inferred dust-obscured star formation. At the same time, investigations of dust-obscured star formation leveraging the Atacama Large Millimeter/submillimeter Array (ALMA) at higher redshifts ($z \sim 4-6$) suggest that galaxies instead exhibit a lower fraction of obscured star formation relative to galaxies today (e.g., Fudamoto et al. 2020; Gruppioni et al. 2020; Algera et al. 2023). Taken together, observations suggest an epoch of $z \sim 4$ as the transition period after which dust-obscured star formation becomes the dominant contributor to the total star formation budget (Casey et al. 2021; Zavala et al. 2021).

Observations from low and high redshift suggest a relatively consistent picture of dust-obscured star formation. At low redshift, a greater fraction of star formation is obscured by dust than for high-redshift galaxies. However, the nature of determining the fraction of dust-obscured star formation observationally is subject to significant uncertainties owing to selection effects; UV/optically selected samples will preferentially be unobscured, and the opposite is true for IR-selected samples. Similarly, different observational tracers for the star formation rate (SFR) in galaxies can result in systematically different inferred values of dust-obscured star formation (e.g., Kennicutt & Evans 2012). As a result, simulations may help to elucidate the situation because they provide self-complete, time-evolving, three-dimensional pictures of galaxies that can connect observational quantities with intrinsic physical properties.

Theoretical work in this area has focused on particular aspects of obscured star formation, and it is often restricted to high redshift. Theoretical studies have explored cosmological simulations (Vogelsberger et al. 2020; Shen et al. 2022; Lewis et al. 2023), zoom-in simulations (Ma et al. 2018;Vijayan et al. 2024), and semi-analytic models (Mauerhofer & Dayal 2023). However, each of these is limited in at least one key aspect necessary to study obscured star formation across cosmic time: (i) the dust is post-processed onto the simulation and therefore not produced in the simulation in a self-consistent manner, (ii) the sample of galaxies is limited, or (iii) the results do not extend to low-redshift comparisons and cannot address the question of how dust-obscured star formation might change with cosmic time. We attempt to address these three limitations in this work.

In this paper, we generate and analyze synthetic observations of galaxy spectra with dust utilizing the SIMBA cosmological simulation to investigate dust-obscured star formation across both the galaxy mass function and cosmic time. We focus on whether we can reproduce observational results and then leverage our simulations to understand the physics driving our results. In Section 2, we present our methodology for producing a mock galaxy spectral energy distribution (SED) sample, and in Section 3, we present our predictions for dust-obscured star formation in our simulation up to $z = 6$ and use our knowledge of the simulation physics to investigate its causes. In Section 4, we provide discussion of our results in context of the literature, and in Section 5, we summarize our work.

2. Methodology

2.1. Simulations

In order to understand the impact of dust obscuration on our knowledge of star formation, we utilize the SIMBA cosmological simulations (Davé et al. 2019) and construct synthetic observations of identified galaxies within SIMBA. Here, we include a summary of the relevant physics in SIMBA. For a full discussion, see Davé et al. (2019).

SIMBA is built off of the GIZMO hydrodynamic code (Hopkins 2015) and is the successor to the MUFASA simulations (Davé et al. 2016). It features a SFR dependent on the H_2 density (Kennicutt 1998), and the produced star particles are assumed to follow a Chabrier initial mass function (IMF; Chabrier 2003). The H_2 mass is determined based on the Krumholz & Gnedin (2011) model. The gas cooling and heating is calculated by the GRACKLE chemistry module (Smith et al. 2017), which includes metal cooling, photoionization, and the self-shielding model of Rahmati et al. (2013) against an ionizing background calculated from the Haardt & Madau (2012) model. Stellar feedback is present in metal-loaded winds that enrich the ISM for future generations of stars; the metal yields for Type II supernovae, Type Ia supernovae, and asymptotic giant branch (AGB) stars are determined using models from Iwamoto et al. (1999), Nomoto et al. (2006), and Oppenheimer & Davé (2006), respectively. Additionally, SIMBA includes black hole growth based on two growth modes: a cold accretion mode based on Anglés-Alcázar et al. (2017), and a hot halo mode based on Bondi & Hoyle (1944). Black hole feedback takes both kinetic and radiative forms; kinetic feedback is jet-based for low accretion and wind-based for high accretion, while radiative feedback is based off of an X-ray model dumping energy into gas. The black hole model for X-ray feedback is derived from Choi et al. (2012).

Importantly, SIMBA features a self-consistent dust production, growth, and destruction model (Davé et al. 2019; Li et al. 2019). SIMBA tracks the presence of 11 elements across cosmic time produced by the enrichment model. All dust grains are assumed to have the same constant size of 0.1 μm and have their motions tied to the gas particles. Dust production is governed by taking fixed fractions of these metals from the enrichment process of Type II supernovae and AGB star production as in the Dwek (1998) model, with newer condensation fractions based on the models of Ferrarotti & Gail (2006) and Bianchi & Schneider (2007). The grains grow by accreting local gaseous metals. Dust is destroyed by thermal sputtering and a subgrid model for supernova shocks (McKinnon et al. 2016). Gas particles can also have their dust destroyed by the models for AGN jet feedback (Anglés-Alcázar et al. 2017), AGN X-ray emission (Choi et al. 2012), winds, and supernova feedback. This model is tuned to reproduce the $z = 0$ dust mass function and is successful in reproducing higher-redshift dust measurements (Li et al. 2019).

We analyze the high-resolution SIMBA m25n512 run—this is a simulated cosmological box with $25/h$ Mpc sides in comoving coordinates that contains 512^3 particles and a mass resolution of $2.3 \times 10^6 M_\odot$ and $1.2 \times 10^7 M_\odot$ for gas and dark matter particles, respectively. The SIMBA cosmology is flat, with $H_0 = 68$ km s^{-1} Mpc^{-1} and $\Omega_{m,0} = 0.3$.

2.2. Simulated Galaxies Sample Selection

We identify galaxies within the SIMBA simulation at redshifts $z = 0.5$ and integer redshifts $z = 1-6$ using CAESAR (Thompson 2014), a package utilizing YT (Turk et al. 2011) and a six-dimensional friends-of-friends (FOF) algorithm, to identify galaxies and dark matter halos. We include $z = 0.5$ rather than $z = 0$ to correspond to the minimum redshift of the data used to produce the fits to obscured star formation in Whitaker et al. (2017). A "galaxy" is defined as a group of bound particles in the simulations featuring a minimum of 16 star particles. The minimum stellar mass of a galaxy is then $\sim 2 \times 10^7 M_\odot$ at each redshift. Dark matter halos are defined similarly, as a group of gravitationally bound FOF-associated dark matter particles. CAESAR also computes relevant quantities such as the stellar mass and dust mass of the identified galaxies. Stellar mass is computed simply by summing the mass of the grouped star particles. In the m25n512 box, CAESAR identifies 1389, 2164, 2989, 3388,

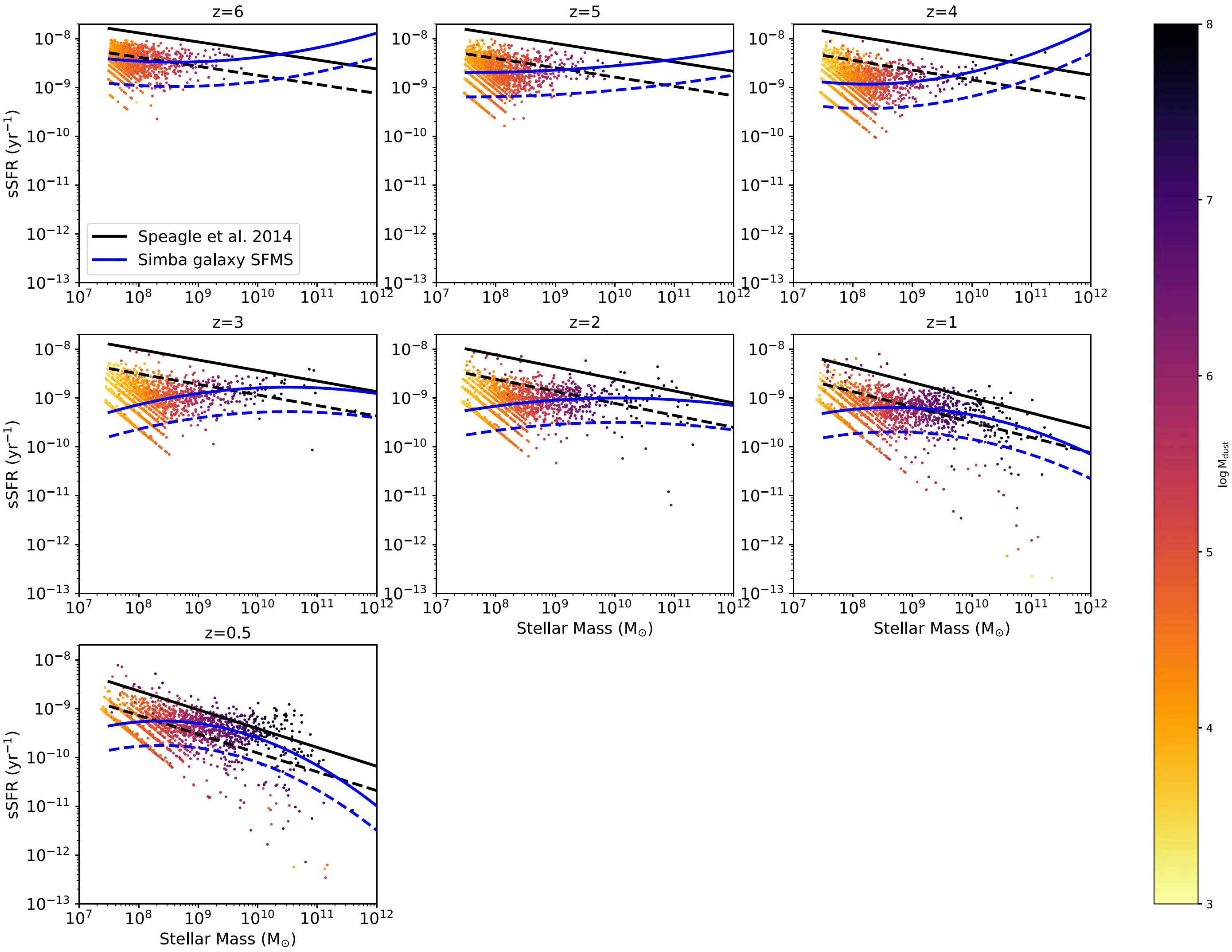

Figure 1. The derived Simba galaxy star formation main sequence (SFMS). The blue lines are quadratic fits similar to the work of Whitaker et al. (2014) and illustrate the SIMBA main sequence and 0.5 dex SF cutoff in solid and dashed lines, respectively. Galaxies above the dashed blue line are labeled as star-forming (SF) and those below are labeled as quenched. Black lines represent the observationally derived Speagle et al. (2014) SFMS for comparison. The striping visible at low SFR reflects the nature of the simulation forming discrete star particles at a fixed mass resolution. The fit for $z = 4$ has an upturn at high masses, but we are focused on a reasonable identification of SF galaxies rather than the precise details of the main sequence.

3788, 4692, and 5372 galaxies under this simple definition at $z = 6$, 5, 4, 3, 2, 1, and 0.5, respectively.

Most observational analyses of obscured star formation limit themselves to galaxies that are actively forming stars. Galaxies that are actively star-forming (SF) will naturally make up the majority of dust-obscured star formation. Additionally, the molecular gas-to-dust mass ratio between low and high specific star formation rate (sSFR) galaxies is expected to be systematically different (Whitaker et al. 2021). We therefore attempt to limit our analysis to SF galaxies within the simulation. We derive the star formation main sequence of galaxies (SFMS) in the SIMBA simulation as in Akins et al. (2022); namely, we iteratively fit a quadratic curve in the shape of Whitaker et al.'s (2014) Equation (2) at each redshift. We define all galaxies more than 0.5 dex in SFR below the fit for a given stellar mass as "quenched." Anything above this cutoff we treat as "star-forming" in this work. Notably, this means that this analysis does not exclude starburst galaxies that are experiencing a large uptick in star formation. We present the derived main sequence in Figure 1.

2.3. Radiative Transfer and SED Processing

The three-dimensional radiative transfer code POWDERDAY (Narayanan et al. 2021) enables the generation of synthetic SEDs for galaxies identified with CAESAR. The package YT is responsible for interfacing with the simulation output (Turk et al. 2011). YT smooths the discrete particles onto a grid using an octree to prepare for the later Monte Carlo radiative transfer step. The stellar spectra are generated with FSPS, assuming that each star particle can be treated as a simple stellar population (SSP; Conroy et al. 2009, 2010). For consistency with SIMBA, we use a Chabrier IMF to generate the SSPs (Chabrier 2003). We use the default MIST isochrones (Paxton et al. 2011, 2013, 2015; Choi et al. 2016; Dotter 2016) and the MILES spectral library (Vazdekis et al. 2010; Falcón-Barroso et al. 2011; Vazdekis et al. 2015). Given the input stellar SEDs from FSPS and the grid from YT, HYPERION performs three-dimensional dust radiative transfer by a Monte Carlo photon-packet-based algorithm and produces a final SED for a galaxy (Robitaille 2011). Photon packets in every iteration are followed as they randomly scatter, are absorbed, or pass through the dust until they either leave the octree grid or are absorbed. The Monte Carlo photon processing stops when 99% of the galaxy octree cells have their dust temperatures and radiation fields change by less than 1% between iterations. The Weingartner & Draine (2001) dust extinction law is used in cells for these SIMBA simulations.

We run POWDERDAY on every galaxy in our model galaxy sample. This enables us to construct a catalog of mock galaxy SEDs across different epochs in the SIMBA simulation. We additionally generate these simulated galaxy SEDs at nine different orientations per galaxy. This allows us to sample different line-of-sight column densities and explore how the fraction of obscured star formation in a galaxy may depend on its orientation. In the Appendix, we discuss the validity of our synthetic spectra and find a reasonable resemblance to real-world galaxies.

3. Results

3.1. Evolution of Obscured Star Formation

We first turn our attention to the fraction of dust-obscured star formation in our cosmological simulations. To determine this fraction from our simulations, we integrate the generated galaxy SEDs in the appropriate wavelength regimes to determine the rest-frame IR and UV luminosities, which we define as the integrated luminosity between 8 and 1000 μm and 1216−3000 Å, respectively. Mirroring the work of Whitaker et al. (2014), we convert to SFRs with the Kennicutt (1998) $L_{\rm IR}$–SFR conversion (Equation (1)) and the Bell et al. (2005) $L_{\rm UV}$–SFR conversion (Equation (2)). We again note that there are many different assumptions that could be made to derive SFR from observations that could introduce systematic differences in results (e.g., Murphy et al. 2011). However, we proceed using those from Whitaker et al. (2014) for the sake of comparisons to observations.

$$\mathrm{SFR_{IR}}(M_\odot/\mathrm{yr}) = 1.09 \times 10^{-10} \times L_{\rm IR}(L_\odot), \tag{1}$$

$$\mathrm{SFR_{UV}}(M_\odot/\mathrm{yr}) = 1.09 \times 10^{-10} \times 2.2 L_{\rm UV}(L_\odot). \tag{2}$$

We compute $f_{\rm obs}$, the "fraction of obscured star formation," via the observationally motivated definition $\mathrm{SFR_{IR}}/(\mathrm{SFR_{IR}} + \mathrm{SFR_{UV}})$. Using the luminosity–SFR conversions, we can directly calculate $f_{\rm obs}$ as in Equation (3):

$$f_{\rm obs} = \frac{L_{\rm IR}}{L_{\rm IR} + 2.2 L_{\rm UV}}. \tag{3}$$

We now examine our main finding of evolution in the fraction of obscured star formation ($f_{\rm obs}$) at $z > 3$. In Figure 2, we compare the stellar mass of our simulated galaxies and their $f_{\rm obs}$ from $z = 0.5$−6 against the observational median trend derived in Whitaker et al. (2017) from galaxy survey observations at $0.5 < z < 2.5$. It is clear that, for our simulation, there is predicted evolution in $f_{\rm obs}$ with time for galaxies of fixed stellar mass; namely, galaxies at a fixed stellar mass are predicted to have more of their star formation obscured by dust at higher redshifts as compared to lower-redshift galaxies. This redshift evolution is more pronounced at high redshifts, with the offset in the median relation from the best fit of Whitaker et al. (2017) only becoming pronounced at $z > 3$. The limited evolution in $f_{\rm obs}$ from $z = 0.5$−3 allows the median simulation trend to be reasonably consistent with the observed fits from Whitaker et al. (2017) at $z = 0.5$−3, but the galaxies deviate from this trend at higher redshift. The higher-mass galaxies diverge from the median relation more strongly at lower redshift than the populations of low-mass galaxies at each redshift. Note that the best-fit observed trend is indicated with a dotted line for $z = 3$−6 owing to the fact that Whitaker et al. (2017) only considered data out to $z = 2.5$. We also see this evolution in Figure 3, where we instead show the median trends in the z–$f_{\rm obs}$ relation in various stellar mass bins for our simulated galaxies at $z = 0.5$, 1, 2, 3, 4, 5, and 6. For virtually all stellar mass bins, the evolution in $f_{\rm obs}$ is steepest up to $z \sim 3$, where the evolution tends to become weak or minimal. The highest-mass bins do not exhibit any apparent evolution in their medians, but the spread in their $f_{\rm obs}$ is clearly higher at low redshift. We note that because of its size, the simulation box does not produce galaxies of these masses at $z > 4$ to compare.

We predict an increase in the dispersion of the $f_{\rm obs}$–M_* relation at lower redshifts. We demonstrate this by comparing the 16th and 84th percentiles of the bins at $z = 0.5$ and $z = 6$ in Figure 2. In Figure 3, this trend is clearly visible for the four most massive mass bins; at redshifts $z < 3$, the dispersions in the mass bins increase significantly for the depicted redshifts.

3.2. Explaining the Evolution of f_{obs}

We have seen that our cosmological simulation exhibits an evolution in the fraction of obscured star formation; galaxies of the same stellar mass have greater fractions of their UV light obscured by dust at higher redshift. With our evolving, self-consistent dust model, we investigate the physical reason for this. At the outset, there are two likely reasons for this evolution: an evolution in the total dust mass at a fixed stellar mass, and/or an evolution in the dust attenuation law (which is a manifestation of evolution in the star-dust geometry assuming a fixed opacity law; Salim & Narayanan 2020). We now investigate these possible physical origins of the evolution of the $f_{\rm obscured}$–M_* relationship with redshift in turn.

3.2.1. Evolution of Dust Mass

One possible explanation for the evolution of $f_{\rm obs}$ with redshift at a fixed stellar mass is via an evolution in galaxy dust masses. Larger quantities of dust would correspond to higher typical column densities along the line of sight and therefore more attenuated starlight in the UV. We find an unsurprising correlation between dust-obscured star formation fraction and dust mass. In Figure 2, we color-code the individual galaxies by their dust mass. Most of the highly obscured galaxies have the highest amount of dust accumulated within them. This is especially notable at lower redshifts, where the intrinsic scatter is larger; many of the simulated galaxies that are outliers to the median trend in obscuration have noticeably higher dust masses than their less obscured counterparts at similar stellar mass. This result is reinforced with Figure 4, where we analyze the median dust-to-stellar mass ratio across redshift and find a strong correlation between stellar mass and dust mass to stellar mass ratio. This correlation can allow us to physically explain the trend of $f_{\rm obs}$ with stellar mass; more massive galaxies in our simulations typically have more dust per stellar mass, which naturally results in higher $f_{\rm obs}$. Observational results such as Magnelli et al. (2020) have also found that high-mass galaxies tend to contain the most dust. However, this does not explain the evolution in $f_{\rm obs}$ with redshift, as Figure 4 exhibits no clear trend with redshift at a fixed stellar mass, excluding the lowest stellar masses at each redshift where we might have concerns

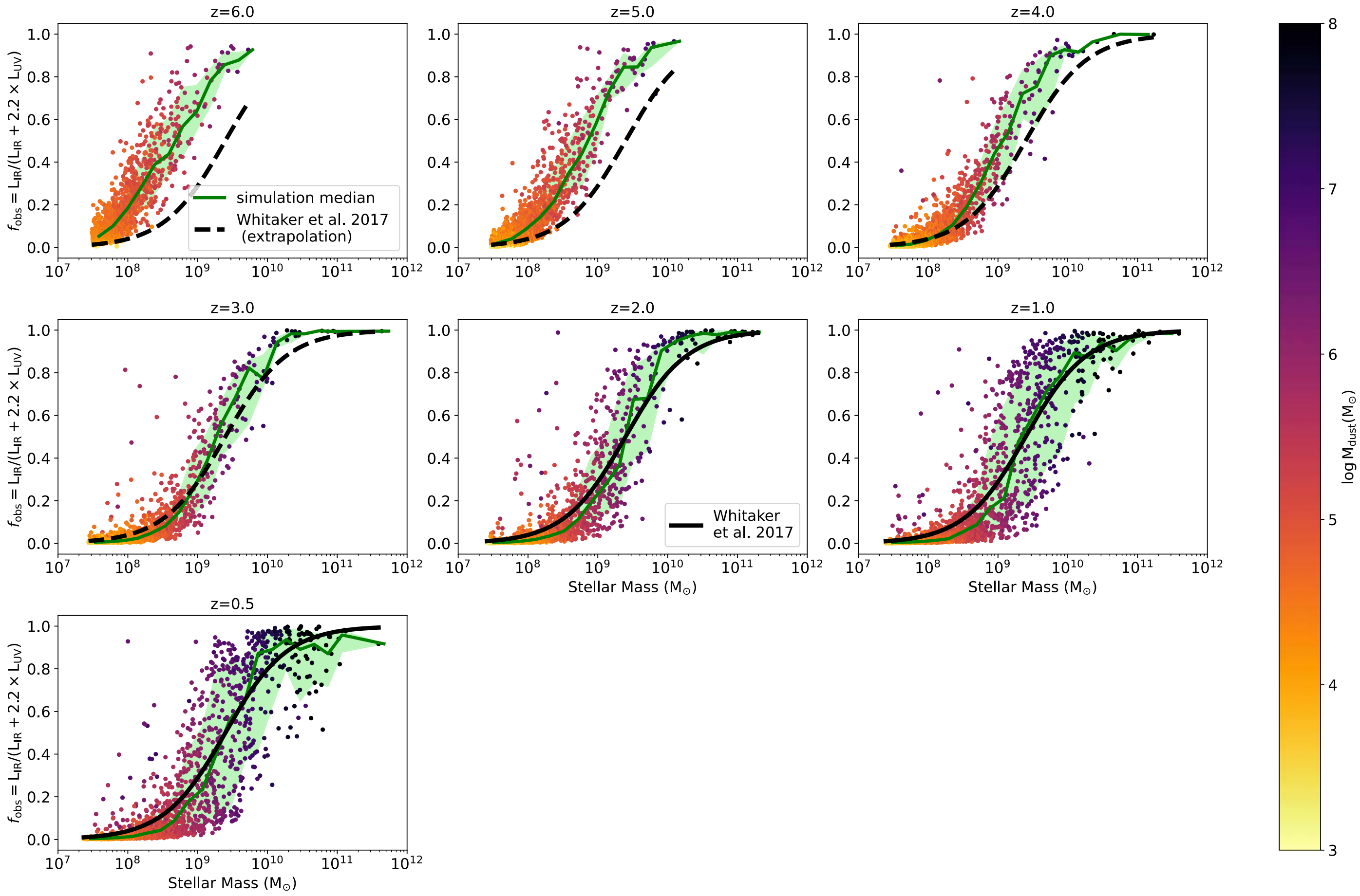

Figure 2. $f_{\rm obs}$, the fraction of obscured star formation in a galaxy, depends on stellar mass and redshift. Here, the green line indicates a log mass-binned median trend with bins of size 0.2 dex in stellar mass, with error bars marked by the shaded regions including the 16th and 84th percentiles of the data within the given bins. The black solid line represents the median trend from observations out to $z = 2.5$ as determined by Whitaker et al. (2017). The black line is instead dashed at redshifts $z > 2.5$ to represent that is an extrapolation of the Whitaker et al. (2017) best fit. There is clear evolution in $f_{\rm obs}$ in galaxies across time; galaxies at fixed stellar mass become less obscured with time. We find the running median for $f_{\rm obs}$ to reasonably follow the Whitaker fit within the redshift range of the observations ($z = 0.5-2.5$), though note that our model predicts evolution in $f_{\rm obs}$ at earlier times.

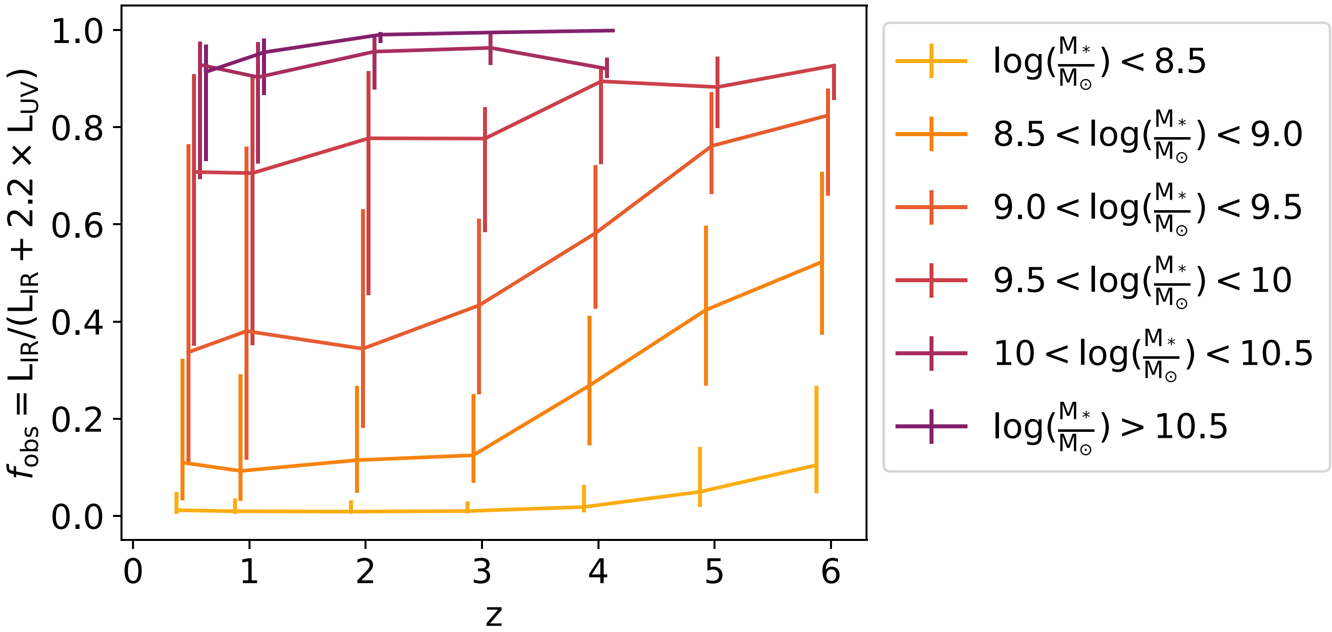

Figure 3. Median relationship between $f_{\rm obs}$ and z as a function of stellar mass. This plot compares $f_{\rm obs}$ against redshifts for a set of six galaxy stellar mass bins. The positions of the medians are slightly offset from the true redshift for the visibility of the dispersion. At higher redshifts, galaxies at a fixed stellar mass are more obscured than their lower-redshift counterparts. These trends are derived by 0.5 dex bins of stellar mass, with the dispersion produced by the 16th and 84th percentiles of the data belonging to the bin.

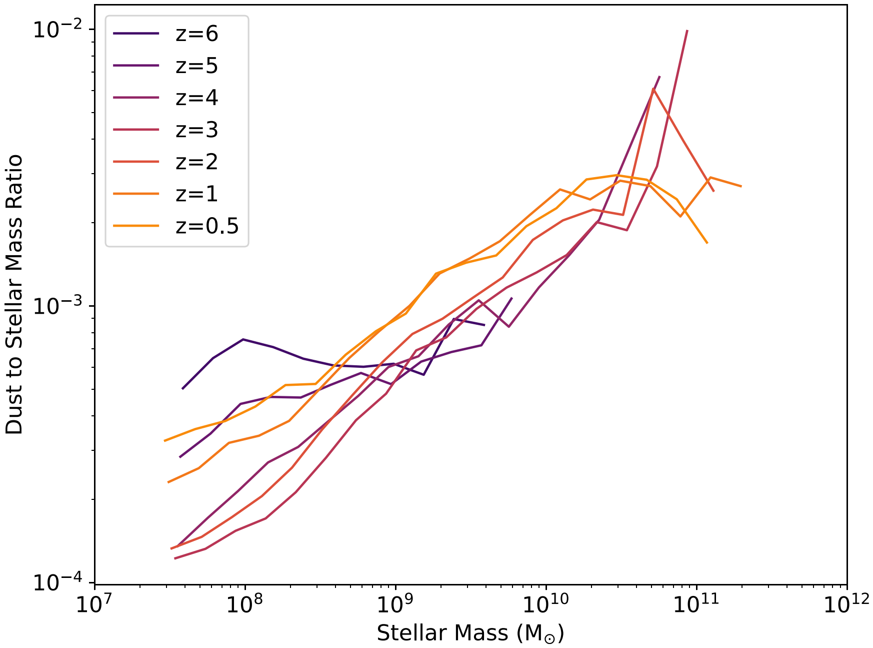

Figure 4. The dust-to-stellar mass ratio explains the dependence of $f_{\rm obs}$ on stellar mass but not the redshift evolution of $f_{\rm obs}$ at fixed stellar mass. Here, we compare the median stellar mass and dust-to-stellar mass ratio at various redshifts. Higher-mass galaxies have higher fractions of dust than lower-mass galaxies. The greater dust fractions also generally correspond with higher $f_{\rm obs}$. However, for fixed stellar mass of higher-mass galaxies, the dust fraction does not evolve strongly with redshift above the lowest stellar masses, which do exhibit noticeable differences.

about the resolution. Redshifts 0.5 and 1 even seem to have the highest dust-to-stellar mass ratios, which would suggest a trend of increased obscuration with decreasing redshift rather than what we observe in Section 3.1. The limited evolution in the median dust-to-stellar mass ratio implies that the dust-to-stellar mass ratio can serve as a proxy for the stellar mass.

In Figure 5, we plot the dust-to-stellar mass ratios for individual galaxies and recover the shape of the M_*–f distribution very clearly at low redshift. The differences at higher redshift are due mainly to the lack of massive galaxies formed and the remainder of the galaxies being in the stellar mass range where there are more pronounced differences in the dust-to-stellar mass ratio. Similarly, Li et al. (2019) find that the dust-to-gas mass ratio at fixed galaxy metallicity in the SIMBA simulation does not vary strongly with redshift. This rules out a change in dust mass with time as an explanation for the strong evolution of the median $f_{\rm obs}$ trend at $z > 2$.

3.2.2. Star-dust Geometry

We now turn to evolution in the star-dust geometry as an explanation for the redshift evolution of the $f_{\rm obs}$–$M_\star$ relation. The general premise here is that two galaxies with the same M_* and $M_{\rm dust}$ but different dust attenuation laws would result in different ratios of IR to UV flux. Star-dust geometry can manifest itself in two manners: galaxy viewing orientation, and ISM clumping. We explore these in turn.

We first explore the effects of orientation on the fraction of obscured star formation. Star-dust geometry would be expected to vary depending on the viewing angle of the galaxy. If high-redshift galaxies in our simulations tend to be less disk-like, then they would have less of a viewing-angle bias in their $f_{\rm obs}$. Conversely, if the fraction of galaxy disks is higher at a given redshift, this would result in a greater spread based on viewing angle and more viewing angles with a lower column density of dust. To test this, we have set up cameras at nine isotropically arranged viewing angles around each galaxy.

In Figure 6, we present the median ratios between the maximum and minimum $f_{\rm obs}$ among these nine orientations for galaxies in the same stellar mass bins used for Figure 3 as well as the values corresponding to the 16th and 84th percentiles in these bins. A value of 1 means there is no dependence on the viewing angle for $f_{\rm obs}$; the greater the value, the more important the viewing angle of the galaxy is to the observed SED. A factor of 2 indicates that $f_{\rm obs}$ is doubled by orienting the galaxy a different way. There is no clear monotonic trend with stellar mass, and the distributions of the ratios are broad for most of the mass bins, especially at low redshift, to the point that any trends with the bin medians overlap with the dispersion of the bins at other redshifts. For the mass bins with $9 < \log M_* < 10$, there is an increase in the orientation dependence of $f_{\rm obs}$ with decreasing redshift up to $z \sim 3$ (with large spreads in the distributions). This indicates that some of the evolution in the spread of $f_{\rm obs}$ for these mass bins can likely be attributed to orientation effects. Notably, the highest-mass bins experience an increase in the median and width of their distribution at low redshift; this again implies that the increased spread in $f_{\rm obs}$ at high masses should at least be partially attributed to orientation effects. Overall, despite the lack of consistent trend in the orientation dependence of $f_{\rm obs}$ across mass bins, the typical increased orientation dependence at the highest masses and broader range of orientation dependence suggests that the orientation is likely responsible for a portion of the increased spread at fixed stellar mass we see in Figure 2.

We now examine the impact of ISM clumping, which we quantify via the UV optical depth. With our knowledge of the intrinsic stellar SEDs before dust radiative transfer, we are able to directly compute the attenuation curves of our simulated galaxies. The optical depths in this paper are calculated by the standard Equation (4), where $I_{\lambda,0}$ represents the intrinsic stellar

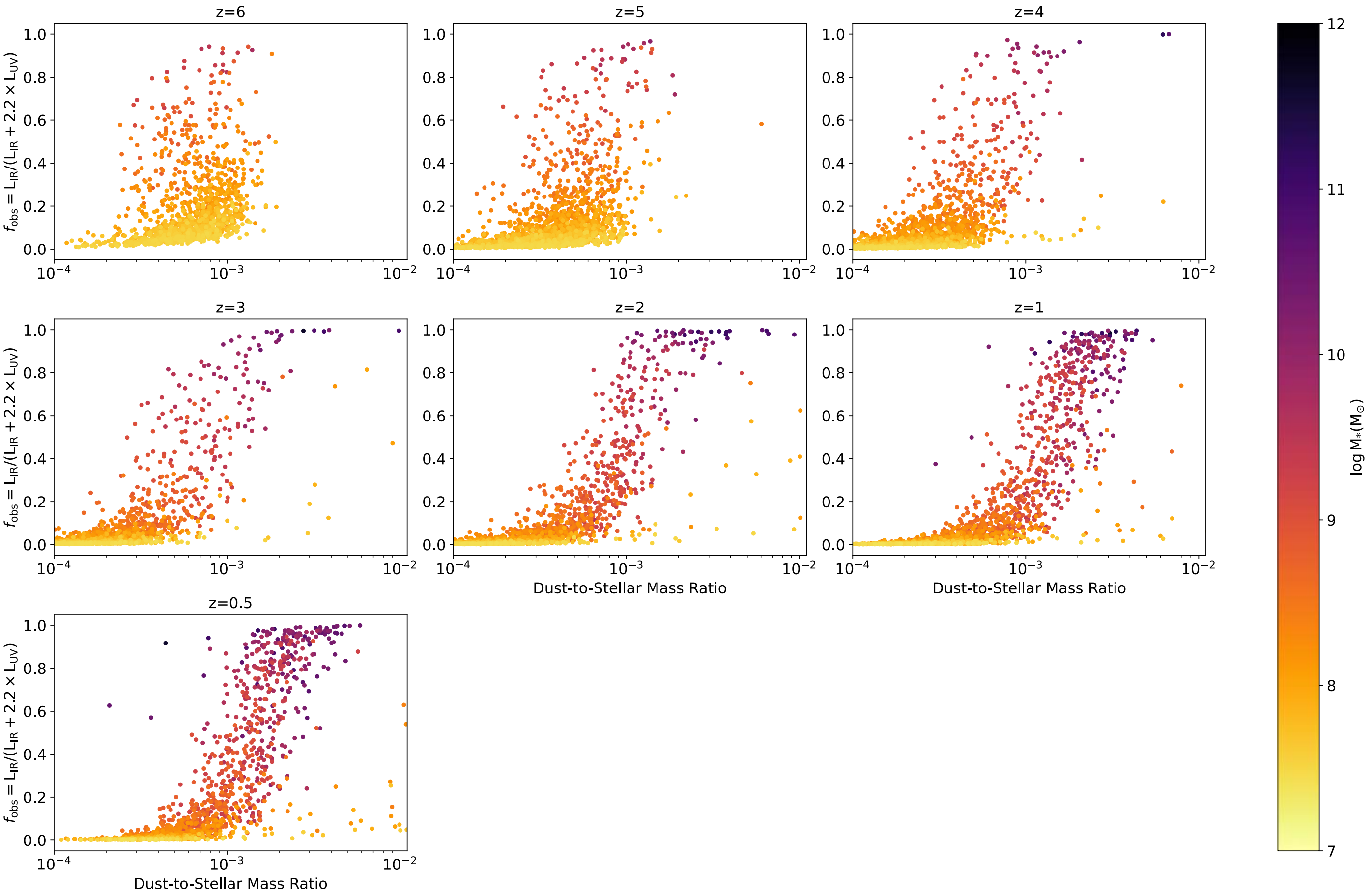

Figure 5. Implications of the lack of strong dust-to-stellar mass ratio evolution for f_{obs} dependence. Following Figure 4, we now compare f_{obs} to the dust-to-stellar mass ratio for our sample of simulated galaxies. Each galaxy is colored by its stellar mass. We do recover the shape of the relation from Figure 2. Galaxies at similar stellar masses do indeed lie in approximately the same ranges of dust-to-stellar mass ratio across redshifts, but their f_{obs} changes. Therefore, the dust-to-stellar mass ratio cannot explain the f_{obs} evolution.

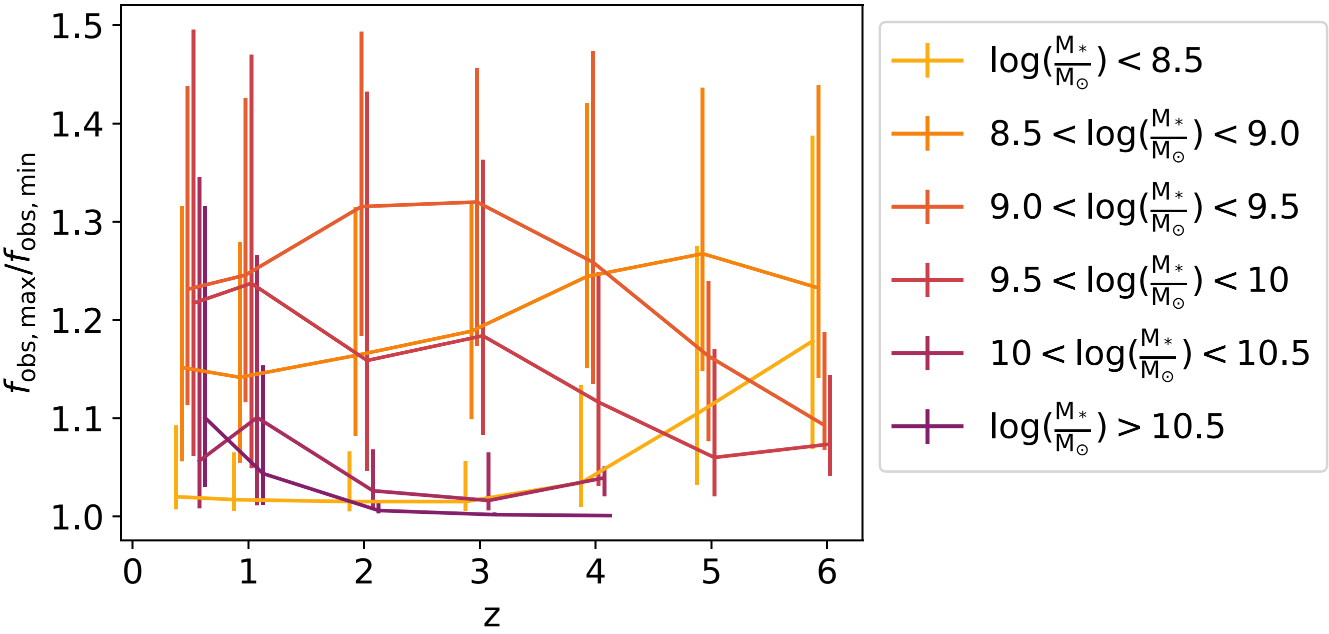

Figure 6. Orientation effects cannot explain the trends in f_{obs} with redshift. We plot for galaxies in various stellar mass bins the median trend for the ratio between the maximum derived f_{obs} and the minimum derived f_{obs} of the nine orientations of the system we run POWDERDAY on. The trends are slightly offset in redshift for the visibility of the distribution spread. High values of this ratio indicate a high dependence of the f_{obs} of the galaxy on the viewing angle of the observer. There is no indication of any consistent trend across different galaxy mass bins.

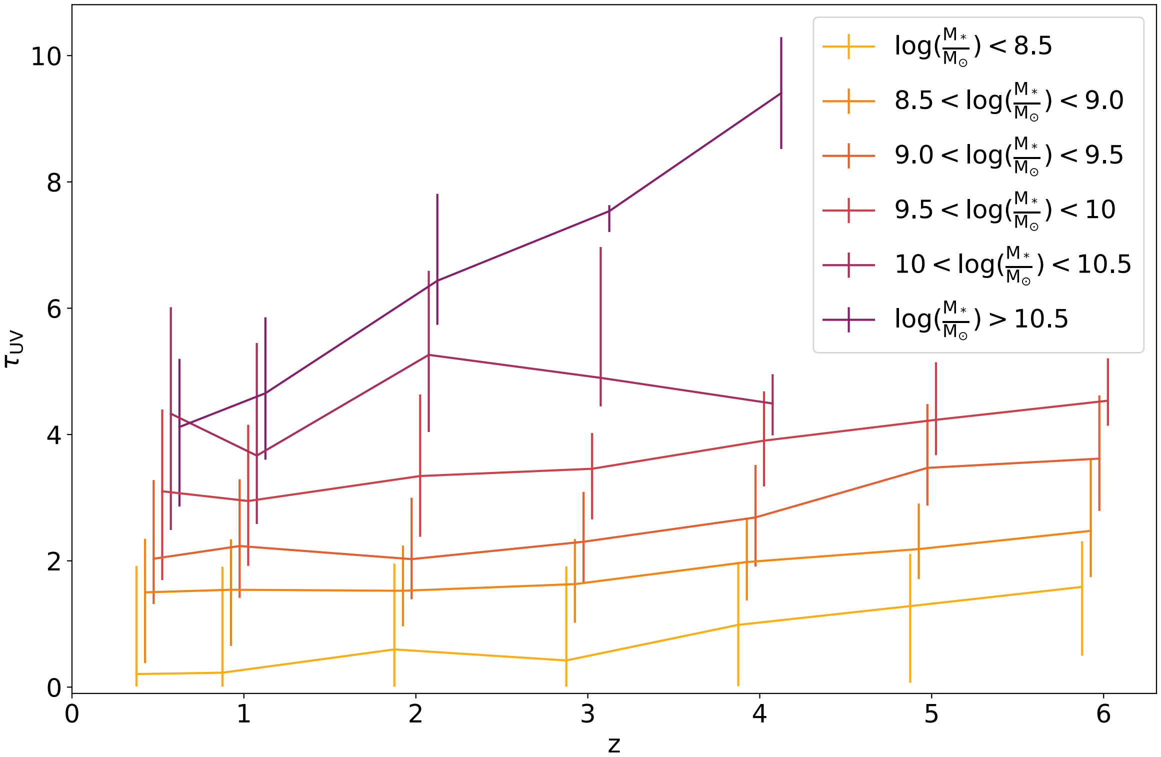

Figure 7. The evolution in UV optical depths explains the evolution of f_{obs} via evolution in star-dust geometries. We plot the median and dispersion of galaxies' optical depths for the wavelength nearest $\lambda = 1500$ Å in the UV for galaxies in different mass bins. We again offset the redshift values for visibility. There is a clear shift in the galaxies across all mass ranges toward lower UV attenuation with lower redshift, which reflects the evolution in obscuration.

SED from the total of the SSP spectra that make up the galaxy produced by FSPS, and I_λ represents the final SED after radiative transfer is performed. We calculate the optical depth at 1500 Å.

$$\tau_\lambda = -\ln \frac{I_\lambda}{I_{\lambda,0}}. \quad (4)$$

In Figure 7, we analyze the optical depths of the galaxies in the UV regime in the range of stellar mass bins discussed so far in this work. We do see a clear shift in the distribution with redshift across all mass bins. The systematically decreasing optical depths with redshift indicate that the column density of dust along the line of sight to young stars is, on average, decreasing with redshift for galaxies of a fixed stellar mass. This change in column density, taken with the lack of evolution in the dust-to-stellar mass ratios, highlights the role of star-dust geometry driving the increased obscuration at high-z. We therefore conclude that the star-dust geometry is playing the main role in our evolution of the obscuration fraction with redshift by the evolution of the dust column densities.

This result is also consistent with the model presented by Shapley et al. (2022) that $\tau_\lambda \propto \kappa_\lambda(M_{dust}/M_{gas})\Sigma_{Gas}$. In our work, the extinction law is constant in each radiative transfer cell, and we have already shown that the dust-to-stellar mass ratio exhibits no evolution; this would assign all evolution in attenuation to the gas surface density term. In Figure 8, we compute the gas surface density as the ratio of the gas mass and the square of the gas half-mass–radius. Indeed, we note that the gas surface density of the simulated galaxies is decreasing with redshift at a fixed stellar mass.

3.3. Obscured Cosmic Star Formation Rate Density

We combine our results for individual galaxies to investigate the contribution of total obscured star formation to the total cosmic star formation rate density (SFRD). We sum and plot the SFR derived from our CAESAR group finder multiplied by the derived f_{obs} for each galaxy to estimate the cosmic fraction of obscured star formation at each redshift. To convert to a SFRD, we divide these results by the comoving volume of the SIMBA m25n512 run. The results are displayed in Figure 9. These correspond to total obscured star formation fractions of 41%, 45%, 75%, 78%, 82%, 74%, and 74% at redshifts $z = 6$, 5, 4, 3, 2, 1, and 0.5, respectively. At $z = 4$, there is a turnover where obscured star formation becomes the main contributor to the cosmic star formation rate density (CSFRD) in the simulation. This qualitatively matches with observational results (Dunlop et al. 2017; Zavala et al. 2021). Additionally, the SIMBA CSFRD appears to reasonably trace the observationally derived SFRD reasonably well out to $z \sim 6$. Importantly, obscured star formation dominates the SFRD budget in the epoch of "cosmic noon"; this suggests that most of the star formation in the history of the Universe is obscured. We attribute this turnover to the relative lack of galaxies sufficiently massive to have large amounts of star formation and be almost entirely obscured despite the higher obscuration at fixed stellar mass at high redshift we found in Section 3.1.

4. Discussion

4.1. Comparisons to Obscured Star Formation Observations

In this section, we place our results for the evolution of the obscured fraction of star formation, f_{obs}, in observational

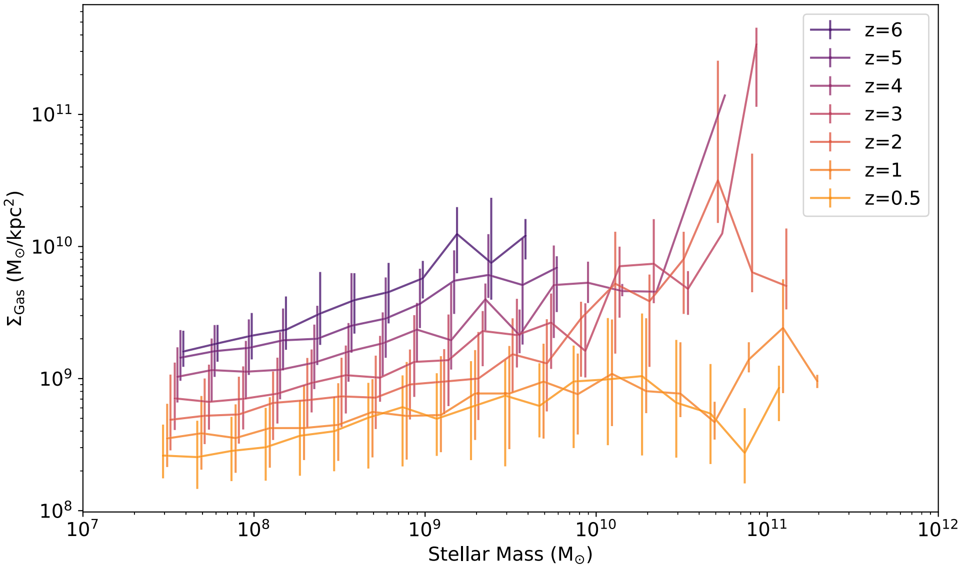

Figure 8. The evolution in the gas surface density corresponds to the evolution in $f_{\rm obs}$. We compute the galactic median trend in surface density across redshifts. We estimate a gas surface density by dividing the gas mass by the square of the radius that encloses half the gas mass. The error bars represent the 16th and 84th percentiles for the galaxies that fall in the bin. There is a clear trend in the gas surface density with time corresponding to decreasing obscuration at constant stellar mass, which follows the explanation presented by Shapley et al. (2022).

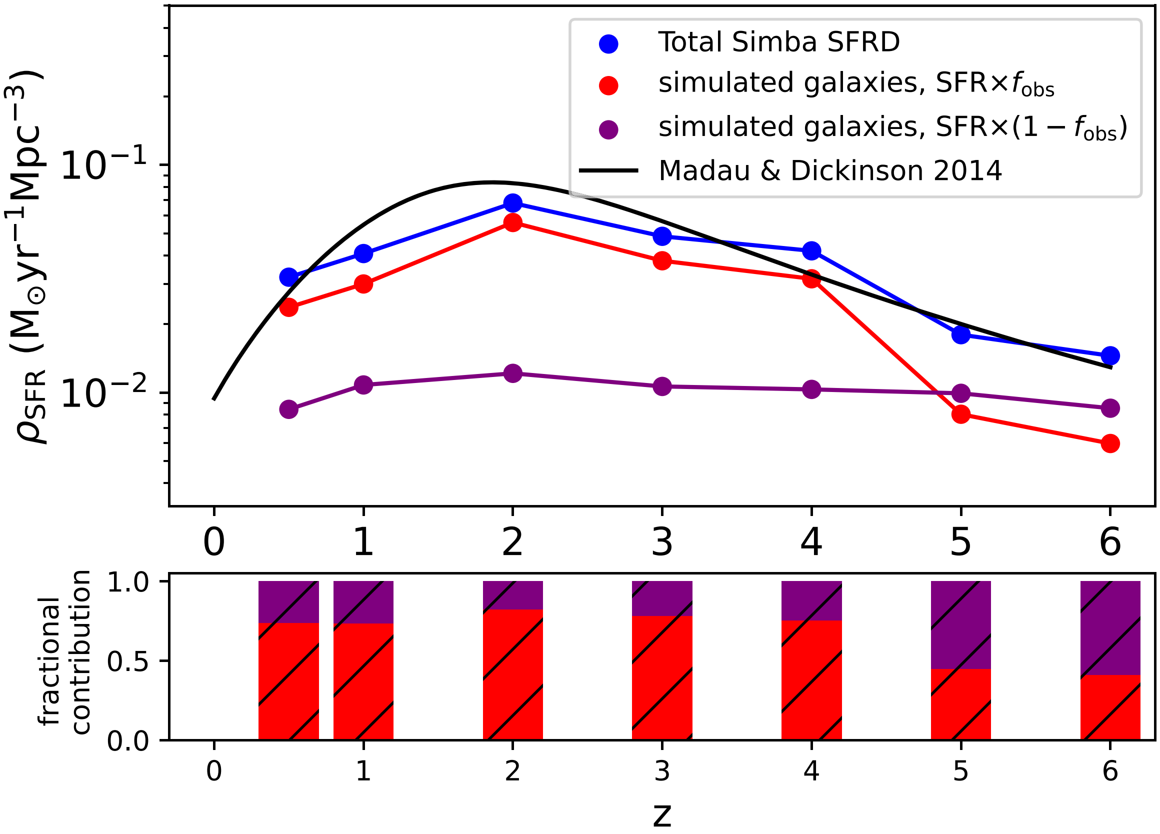

Figure 9. Most obscured star formation dominates the SFR budget of the Universe below $z = 4$. We plot the SFRD across cosmic time in the SIMBA simulations. We break up the galaxies' SFR averaged over 100 Myr into total obscured and unobscured star formation by using the $f_{\rm obs}$ calculated in Section 3.1. Total obscured star formation makes up 41%, 45%, 75%, 78%, 82%, 74%, and 74% of the SFRD at redshifts $z = 6$, 5, 4, 3, 2, 1, and 0.5, respectively. After $z \sim 4$, the obscured star formation dominates the total SFRD. The behavior of the total SFRD roughly traces the fit from Madau & Dickinson (2014). The Madau & Dickinson (2014) SFR trend is scaled to a Chabrier IMF by the conversion factor 0.63 as described in their work.

context. We conclude that there is evolution in the $f_{\rm obs}$ across cosmic time, though the change does not appear significantly different from previous results up to $z \sim 3$.

Our results are consistent with observations of $f_{\rm obs}$ at lower redshift. Whitaker et al. (2017) studied surveys of SF galaxies selected by color up to redshift $z \sim 2.5$ using the same $L_{\rm UV}$–SFR and $L_{\rm IR}$–SFR conversions referenced in this paper. Whitaker et al. (2017) find no significant evolution in $f_{\rm obs}$ in this redshift range; similarly, our results show only mild evolution of $f_{\rm obs}$ in this range. Therefore, our results could be

Table 1
Best-fit Parameters for Equation (5) for the Obscured Fraction of Star Formation as a Function of the Galactic Stellar Mass across Different Redshifts from Simulation Results

z	a	b
6	1.8×10^{9}	−2.5
5	3.5×10^{10}	−2.8
4	9.2×10^{10}	−2.8
3	2.6×10^{11}	−2.8
2	8.0×10^{10}	−2.7
1	8.4×10^{9}	−2.4
0.5	4.3×10^{9}	−2.4
Whitaker et al. (2017)	1.96×10^{9}	−2.277

Note. We include the results from Whitaker et al. (2017) for comparison.

seen as consistent with the Whitaker observations at these lower redshifts and a prediction for greater $f_{\rm obs}$ for galaxies that exist in the first few billion years. For further comparison, we fit our model results of $f_{\rm obs}$–M_* with the form of Equation (5) and present these best-fit parameters in Table 1. We note that differences in our best fits are likely caused by the presence of galaxies that have stellar masses $\lesssim 10^9\,M_\odot$ in our samples. It is clear from Figure 2 that the lower-mass end of our simulated galaxy sample is typically underpredicting $f_{\rm obs}$ relative to the best-fit relation from Whitaker et al. (2017) for the redshifts of the observational data ($z \lesssim 3$). This is unsurprising, as Whitaker et al. (2017) state that the observational galaxy sample that they use is only mass complete down to $10^{9.3}\,M_\odot$ at $z = 1$ and $10^{8.7}\,M_\odot$ at $z = 2.5$.

$$f_{\rm obs} = \frac{1}{1 + a e^{b \log M_*/M_\odot}}. \quad (5)$$

Our results are similarly comparable to other studies for low-redshift obscured star formation. Shapley et al. (2022) explore the lack of evolution through attenuation curves and compare the SDSS $z \sim 0$ to the MOSDEF $z \sim 2.3$ sample, and also find no significant evolution in obscured star formation. A similar parameter to $f_{\rm obs}$ that is derived from galactic observations is the “infrared excess” (IRX), defined in Equation (6). Bouwens et al. (2016) present a best fit to the IRX at all times in the form of Equation (7), combining several studies of galaxies from $z \sim 2$–3. Bouwens et al. (2016) also conclude that the relation between stellar mass and the observed IRX does not evolve significantly over cosmological time if they assume dust temperature evolution with redshift. Given that the IRX is comprised of the same quantities as the $f_{\rm obs}$, we also see evolution in the IRX–M_* relation in the SIMBA simulations (see Figure 10). Our distribution of simulated galaxy luminosities again only starts to show strong divergence from the Bouwens et al. (2016) trend at higher redshift. In follow-up work, Bouwens et al. (2020) use the data from a much larger sample of UV-selected submillimeter galaxies from Dudzevičiūtė et al. (2020) to further study obscured star formation. These data include results up to $z \sim 10$. However, they do not conclude that there is evolution in the M_*−IRX relation for their two redshift bins again and find a median relation that is consistent with their previous work. There is naturally a tension between these results and our work, but it is possible that this tension is a result of the UV-selected sample.

$$\mathrm{IRX} = \frac{L_{\rm IR}}{L_{\rm UV}} \quad (6)$$

$$\log_{10} \mathrm{IRX} = \log_{10} \frac{M_*}{M_\odot} - C. \quad (7)$$

Contrary to our results, observational studies of higher-redshift galaxies tend to find $f_{\rm obs}$ to be lower than the previously discussed low-z observations, which is in direct tension with our findings. The results from the ALPINE survey at higher redshift suggest that the typical $f_{\rm obs}$ of galaxies at fixed stellar mass is actually lower (Fudamoto et al. 2020; Khusanova et al. 2021). This may be due to observational selection effects. For example, the ALPINE survey was based off of a set of rest-UV-selected galaxies; this inherently would bias the resultant sample to galaxies with lower $f_{\rm obs}$. Pope et al. (2017, 2023) find a $2 \times 10^9\,M_\odot$ lensed galaxy at $z \sim 4$ with similarly high $f_{\rm obs}$ (∼80%) to the more obscured galaxies in our analogous mass and redshift bin. Williams et al. (2024) suggest that ALMA and Hubble do not observe a significant population of obscured galaxies. Observations by JWST should provide updated estimates for the contributions of obscured galaxies and will serve as a test for our predictions.

4.2. Cosmic Star Formation Rate Density versus Observations

We now turn to comparing our results for the obscured CSFRD against observational results. The SFRD of the SIMBA simulation m25n512 box reasonably traces the observational results, both in terms of qualitative behavior over cosmic time of the SFRD and the turnover between the dominance of obscured and unobscured star formation at $z \sim 4$ (Dunlop et al. 2017; Zavala et al. 2021).

Casey et al. (2018) discuss two potential extreme models for the buildup of dusty galaxies in the early universe: a “dust-poor” early universe, and a “dust-rich” early universe. The dust-poor model involves dusty galaxies only becoming the major contributor to star formation at cosmic noon; the dust-rich model instead involves dusty starbursts playing the main role at redshifts $z > 6.5$ while dusty galaxies would be the main contributors in the range of $1.5 < z < 6.5$. Our predictions include aspects from both of these models, though they favor a universe more closely resembling the dust-rich model. At all redshifts in this work, the 100 galaxies with the greatest star formation contribute the majority of star formation in the simulation (like the dust-rich model). However, it is around cosmic noon where the the total star formation can largely be attributed to the galaxies with the most active star formation (like the dust-poor model). Additionally, we predict that obscured star formation is dominant starting at $z = 4$ only despite the fact that our high-z galaxies are highly obscured rather than UV bright. These differences in our results likely could be used to inform constraints on the parameter space in the Casey et al. (2018) model.

Dunlop et al. (2017) use deep ALMA data corresponding to the Hubble Ultra Deep Field to identify a total of 16 galaxies in the 1.3 mm range. All galaxies they identify have estimated stellar masses $\gtrsim 10^{9.6}\,M_\odot$. Using these extreme galaxies, they identify a turnover at $z \sim 4$ where dust-obscured star formation contributes to the majority of the total star formation. They offer the explanation that the high contribution to obscured galaxies is not dependent on the total dust mass, but instead on

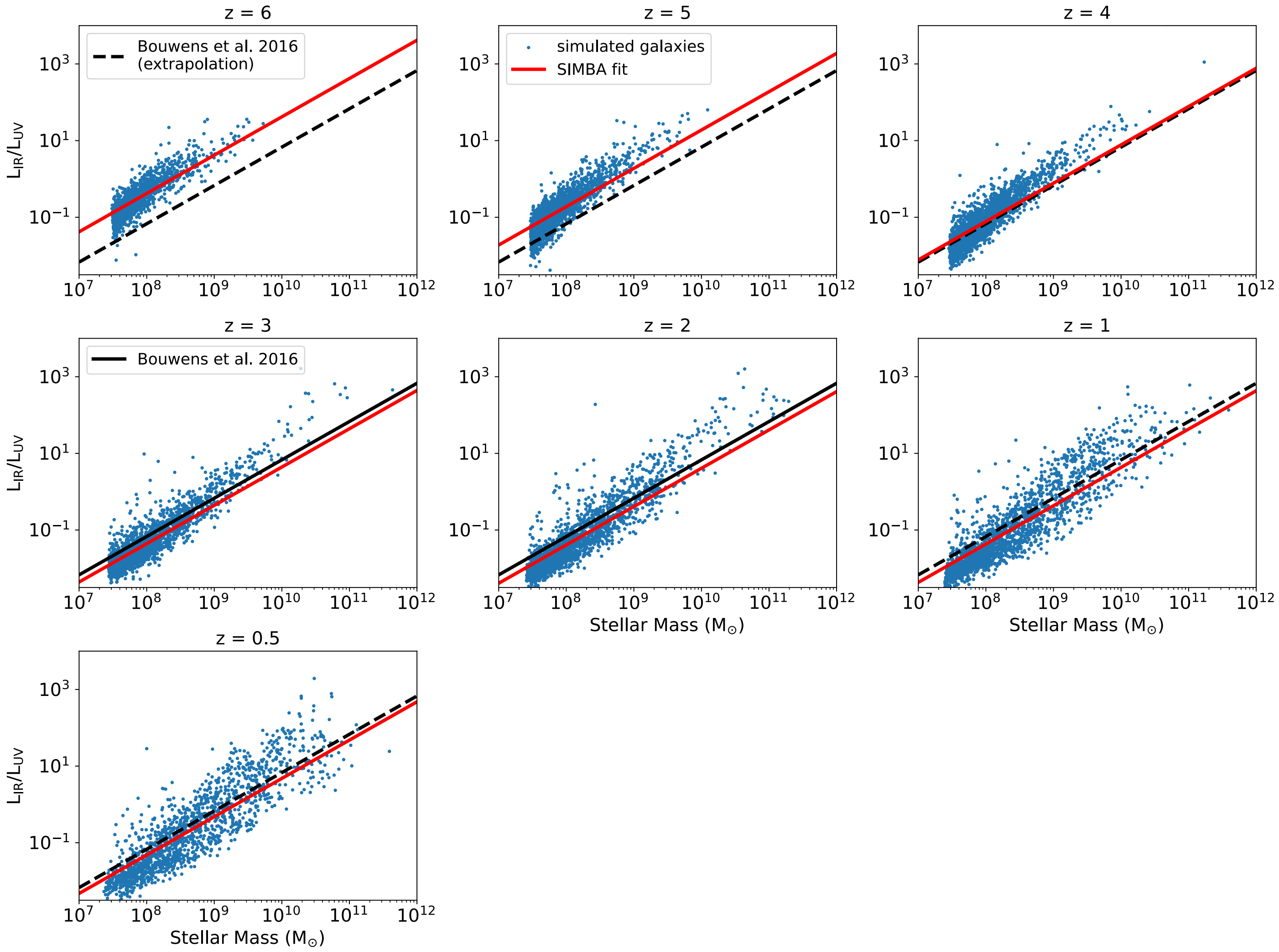

Figure 10. Other expressions of obscured star formation are also inconsistent with the notion of constant obscuration at higher redshift. The IRX–M_* best-fit relation we derive and the values for individual galaxies are plotted against z and compared to the Bouwens et al. (2016) fit derived from a collection of observed $z \sim 2$–3 galaxies as a solid black line at those redshifts. Similar to the fraction of obscured star formation, the distribution of our simulated data at each redshift is reasonably consistent with this fit out to $z \sim 3$, and differs noticeably at higher redshifts. The line is again dashed at redshifts where applying the observational fit would represent an extrapolation.

the fast growth of higher-mass galaxies that contain most of the star formation around and before cosmic noon. Our results generally agree with this notion; as discussed, we do not find a strong dependence of the dust mass on redshift at fixed stellar mass, and we see several massive galaxies around the epoch of cosmic noon with incredibly high SFRs that contribute significantly to the total SFR.

Bouwens et al. (2020) complement their study of the mass–obscuration relation with predictions for the relative amounts of unobscured and obscured star formation up to $z \sim 10$. They find the turnover between obscured and unobscured star formation to occur at $z \sim 5$, which is slightly earlier than we predict. The details of their results could be affected by many necessary assumptions that go into their modeling: the dust temperature evolution, the inference of stellar masses, and the UV-selected nature of their sample.

High-redshift individual galaxy detections such as Fudamoto et al. (2021) have detected early-time, dusty, SF galaxies. Fudamoto et al. (2021) estimate that obscured star formation at $z > 6$ could be contributing between 10% and 25% to the total density. However, Gruppioni et al. (2020) in the ALMA ALPINE survey identify higher fractions of obscured star formation using a larger sample of ∼50 detected IR sources. The contributions to the total SFRD budget from our sample of galaxies better reflect the results of the Gruppioni et al. (2020) work.

4.3. Comparisons to Other Theoretical Models for Obscured Star Formation

We now compare our results for obscured star formation to other theoretical works. Pallottini et al. (2022) modeled zoom simulations of high-redshift galaxies ($z \sim 7.7$), which include many obscured galaxies with high SFRs. They assign dust to their simulated galaxy by assuming a dust-to-metals ratio of 0.08 for their high-redshift galaxies, which is roughly similar to the lower end of the metallicity range of a typical SIMBA galaxy at $z = 6$ in this study; we note, however, that most of our galaxies, especially the most massive in the $z = 6$ sample, have dust-to-metals ratios higher than this assumed value. From spectra of their galaxies, Pallottini et al. (2022) compute the IRX–β relation and find that much of the star formation is heavily obscured by dust despite relatively low attenuation on average. These results further underscore the importance of star-dust geometry to the overall results. The upper end of the range in stellar mass in their sample is relatively analogous to our results, but we have a large sample of $z = 6$ galaxies with IRX ~ 0.1, while their galaxy sample has a minimum IRX of $\sim$1, and we fail to produce any galaxies with IRX $\sim 10^2$ that their sample has. We find that our obscured galaxies at high redshift do typically have high average optical depths, so the low attenuation discussed in Pallottini et al. (2022) is in tension with our results. The likely main causes of this strong tension are the details of the dust model and the difference in resolution between the cosmological SIMBA simulation and the zoom-in SERRA simulation as well as the redshift that is being studied.

Several theoretical works have presented predictions for the contribution of obscured star formation to the total star formation budget at high redshift. The study of Shen et al. (2022) investigates obscured star formation via forward modeling the IllustrisTNG simulation assuming a constant dust-to-metals ratio that evolves with redshift at $z = 4$, 6, and 8 in the form of $0.9 \times (z/2)^{-1.92}$. This translates to a ratio of $\approx$0.11 and 0.24 at $z = 6$ and $z = 4$, respectively. Again, the dust-to-metals ratio for $z = 6$ that they use is on the lower end of the range of values found in SIMBA at this redshift; most of our galaxies have higher dust-to-metals ratios than this. The $z = 4$ value is roughly similar to what a $\sim 10^9\, M_\odot$ stellar mass galaxy typically has in our SIMBA sample at $z = 4$. Our less (more) massive galaxies typically have lower (greater) dust-to-metals ratios than this. They find that they underpredict the abundance of the most IR-luminous galaxies. Using the Murphy et al. (2011) conversion, Shen et al. (2022) find roughly equal contributions of unobscured and obscured star formation at $z \sim 4$ (estimated based on their Figure 8) and predict unobscured star formation to be dominant for $z \gtrsim 4$. This is in keeping with our results; both works lack a sample of high-redshift, high-$L_{\rm IR}$ galaxies and find obscured star formation to be subdominant at very high redshift.

Other theoretical predictions for obscured star formation at individual high redshifts typically are in reasonable agreement with our results. Mauerhofer & Dayal (2023) build a semi-analytic model for galaxy and dust evolution and generate UV and IR luminosities by assuming a single dust grain type and size and a dust geometry that produces a UV photon escape fraction. They predict 34% of star formation to be obscured at $z = 5$, which is slightly lower than our results. Ma et al. (2018) present FIRE-2 zoom simulation results. Their spectra are generated by a combination of stellar population synthesis models assuming a dust-to-metals ratio of 0.4, high relative to virtually all galaxies in our $z = 6$ sample in SIMBA, for Small Magellanic Cloud–like dust. They find 37% of UV light from bright galaxies to be obscured at $z = 6$. This is similar to the results we discuss in this paper. Lewis et al. (2023) run a simulation with a dust production/destruction model included and generate spectra for their halos by taking the intrinsic spectra and computing the extinction along the line of sight for each halo. They calculate the overall fraction of obscured star formation and predict $\sim$45% to be obscured at $z = 5$ and $\sim$40% at $z = 6$ from a magnitude-cut sample of galaxies; our results align very closely with these predictions. Our dust model's differences from the dust models of these theoretical works likely accounts for many of the differences in our results. For example, Esmerian & Gnedin (2024) show that different dust production models alone for the same base cosmological simulation can systematically alter dust masses and effective optical depths, and therefore change the derived obscuration. It is then surprising the extent to which these different simulation strategies agree.

5. Summary

We utilized the galaxies from the SIMBA simulation in redshifts from $z = 0.5$ to $z = 6$ coupled with synthetic POWDERDAY SEDs to study the fraction of obscured star formation $f_{\rm obs}$ throughout cosmic time.

1. We find significant evolution in the fraction of obscured star formation at $z > 3$. Star-forming galaxies at fixed stellar mass are more obscured at higher redshifts, and the spread in $f_{\rm obs}$ along the median trend decreases with increased redshift (Section 3.1, Figure 2). This trend is in tension with some observational studies that mainly find less obscured star formation at high redshifts.
2. We explain the observed trend between $f_{\rm obs}$ and stellar mass at fixed redshift by the increasing dust-to-stellar mass ratios at higher galactic stellar mass (Section 3.2.1, Figure 4). This behavior is present at all redshifts we explore.
3. As the dust mass does not strongly evolve at fixed stellar mass with redshift for our sample of simulated galaxies despite changing $f_{\rm obs}$, we explain the evolution in $f_{\rm obs}$ through evolving star-dust geometry. The column density of dust along the line of sight to young stars is decreasing on average with time (Section 3.2.2, Figure 7) for all galaxy stellar masses. Additionally, our results suggest that the increased spread at fixed stellar mass for $f_{\rm obs}$ can partially be attributed to the orientation dependence of $f_{\rm obs}$ for low-redshift galaxies.
4. Obscured star formation is the dominant contributor across the epoch of cosmic noon to the total star formation budget, with a turnover corresponding to $z \sim 4$, similar to observational results (Section 3.3, Figure 9). This evolution does not conflict with the evolving relationship between stellar mass and $f_{\rm obs}$ because few of the most massive, highly obscured galaxies exist at high redshift. Our results for the overall fraction of obscured star formation match well with predictions from other simulations for high redshift.
5. The evolution in $f_{\rm obs}$ is weak enough at lower redshifts to agree with previous observational results studying lower redshifts ($z \lesssim 3$), which find no significant evolution in obscuration over most of cosmic time (Section 4.1).

Acknowledgments

This work is funded by NSF AST-1909153. D.N. additionally thanks the Aspen Center for Physics, which is supported by National Science Foundation grant No. PHY-1607611, which is where the original framework for the POWDERDAY code base was developed. We thank the anonymous referee for their useful comments.

Appendix
Validity of the Simulations

In this appendix, we attempt to demonstrate that our simulated sample of galaxies and SEDs reflect the real Universe. To this end, at each redshift we study, we investigate the IRX–β relation. The IRX–β is an empirical relation comparing the IRX and the slope of a power-law fit to the UV portion of a galaxy spectrum. The IRX represents the obscuration of starlight, and the β value reflects a combination of the dust attenuation and the underlying stellar populations (Narayanan et al. 2018; Salim & Narayanan 2020). If our simulated galaxies follow the observationally measured IRX–β relation, this then implies that the galaxies in our simulations may have reasonably accurate star-dust geometries and stellar populations as compared to observed galaxies.

To compute the value of β to construct our simulated IRX–β relation, we generate fits for our synthetic SEDs. As with the observationally derived IRX–β relation, we assume that the UV flux can be modeled with a power law $f_\lambda \propto \lambda^\beta$. From the complete spectra, we extract the photometric fluxes corresponding to the wavelengths from the means of the Calzetti et al. (1994) UV windows. We then fit a power law as a function of λ with an exponent (β) and normalization to these select wavelengths and fluxes. This avoids biasing the derived slope due to the 2175 Å bump. To compute IRX, we directly integrate the spectrum to calculate $L_{\rm IR}$ and $L_{\rm UV}$, as described in Section 3.1. We plot the results of the fits for each galaxy as points in Figure 11. For comparison, we plot the Meurer et al. (1999) relation as scaled to the full IR spectrum in Bouwens et al. (2016). By and large, our model galaxies reasonably correspond with the Meurer et al. (1999) locally calibrated relation, suggesting reasonable star-dust geometries and stellar populations in our simulations.

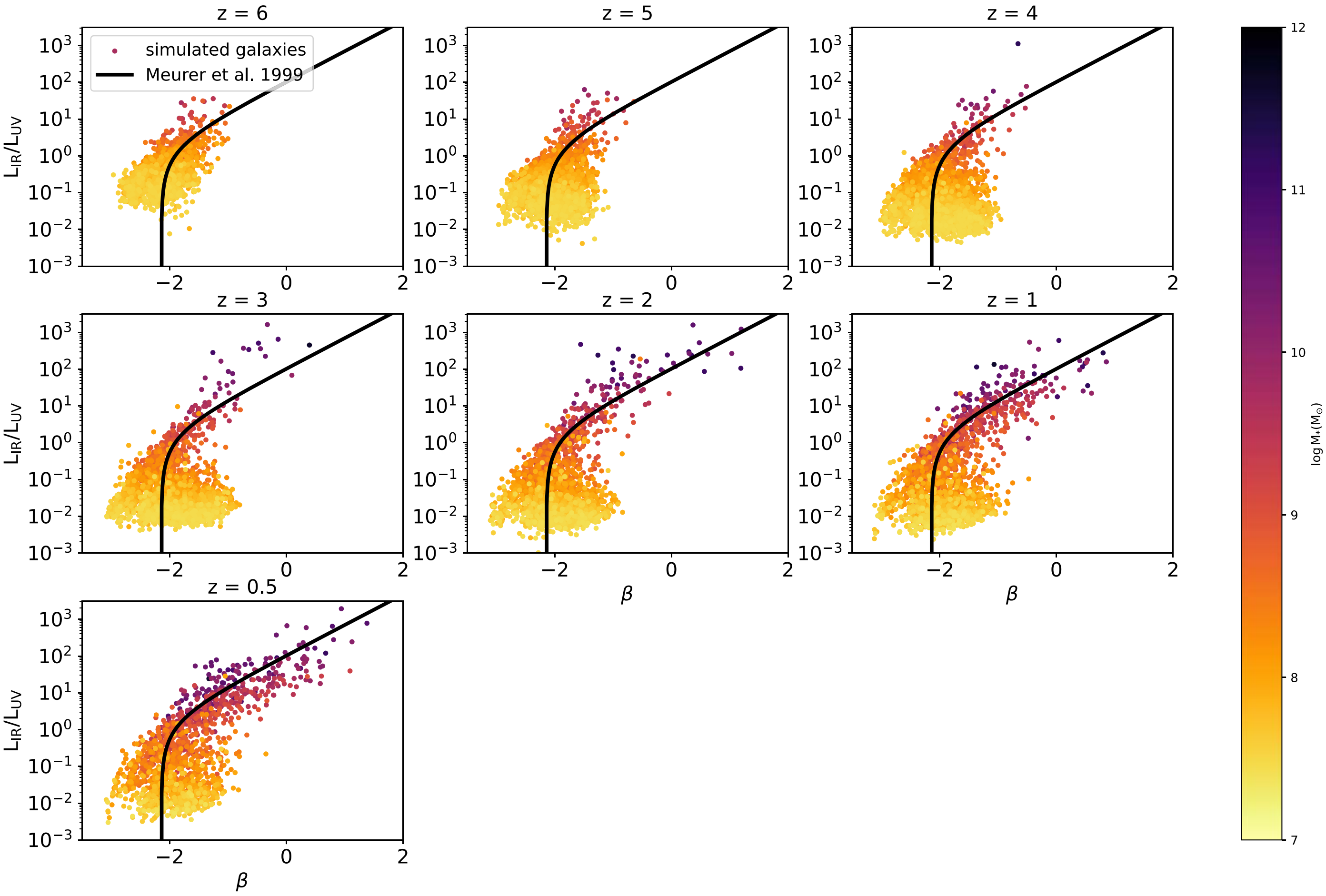

Figure 11. Comparison of simulated data to the locally calibrated IRX–β relation. We plot the IRX–β relation for our sample of simulated galaxy spectra for the redshifts we study and compare to the classic Meurer et al. (1999) relation as scaled by Bouwens et al. (2016) for the full $L_{\rm IR}$. We see the distribution of our simulated galaxies following the Meurer et al. (1999) relation reasonably well across the redshift we study.

ORCID iDs

Dhruv T. Zimmerman https://orcid.org/0009-0008-7017-5742
Desika Narayanan https://orcid.org/0000-0002-7064-4309
Katherine E. Whitaker https://orcid.org/0000-0001-7160-3632
Romeel Davé https://orcid.org/0000-0003-2842-9434

References

Akins, H. B., Narayanan, D., Whitaker, K. E., et al. 2022, ApJ, 929, 94
Algera, H. S. B., Inami, H., Oesch, P. A., et al. 2023, MNRAS, 518, 6142
Anglés-Alcázar, D., Davé, R., Faucher-Giguère, C.-A., Özel, F., & Hopkins, P. F. 2017, MNRAS, 464, 2840
Bell, E. F., Papovich, C., Wolf, C., et al. 2005, ApJ, 625, 23
Bianchi, S., & Schneider, R. 2007, MNRAS, 378, 973
Bondi, H., & Hoyle, F. 1944, MNRAS, 104, 273
Bourne, N., Dunlop, J. S., Merlin, E., et al. 2017, MNRAS, 467, 1360
Bouwens, R., González-López, J., Aravena, M., et al. 2020, ApJ, 902, 112
Bouwens, R. J., Aravena, M., Decarli, R., et al. 2016, ApJ, 833, 72
Calzetti, D., Kinney, A. L., & Storchi-Bergmann, T. 1994, ApJ, 429, 582
Casey, C. M., Zavala, J. A., Manning, S. M., et al. 2021, ApJ, 923, 215
Casey, C. M., Zavala, J. A., Spilker, J., et al. 2018, ApJ, 862, 77
Chabrier, G. 2003, PASP, 115, 763
Choi, E., Ostriker, J. P., Naab, T., & Johansson, P. H. 2012, ApJ, 754, 125
Choi, J., Dotter, A., Conroy, C., et al. 2016, ApJ, 823, 102
Conroy, C., Gunn, J. E., & White, M. 2009, ApJ, 699, 486
Conroy, C., White, M., & Gunn, J. E. 2010, ApJ, 708, 58
Davé, R., Anglés-Alcázar, D., Narayanan, D., et al. 2019, MNRAS, 486, 2827
Davé, R., Thompson, R., & Hopkins, P. F. 2016, MNRAS, 462, 3265
Dotter, A. 2016, ApJS, 222, 8
Dudzevičiūtė, U., Smail, I., Swinbank, A. M., et al. 2020, MNRAS, 494, 3828
Dunlop, J. S., McLure, R. J., Biggs, A. D., et al. 2017, MNRAS, 466, 861
Dwek, E. 1998, ApJ, 501, 643
Elmegreen, B. G., & Scalo, J. 2004, ARA&A, 42, 211
Esmerian, C. J., & Gnedin, N. Y. 2024, ApJ, 968, 113
Falcón-Barroso, J., Sánchez-Blázquez, P., Vazdekis, A., et al. 2011, A&A, 532, A95
Ferrarotti, A. S., & Gail, H. P. 2006, A&A, 447, 553
Fudamoto, Y., Oesch, P. A., Faisst, A., et al. 2020, A&A, 643, A4
Fudamoto, Y., Oesch, P. A., Schouws, S., et al. 2021, Natur, 597, 489
Gruppioni, C., Béthermin, M., Loiacono, F., et al. 2020, A&A, 643, A8
Haardt, F., & Madau, P. 2012, ApJ, 746, 125
Hopkins, P. F. 2015, MNRAS, 450, 53
Iwamoto, K., Brachwitz, F., Nomoto, K., et al. 1999, ApJS, 125, 439
Kennicutt, R. C., & Evans, N. J. 2012, ARA&A, 50, 531
Kennicutt, R. C., Jr. 1998, ApJ, 498, 541
Khusanova, Y., Bethermin, M., Le Fèvre, O., et al. 2021, A&A, 649, A152
Krumholz, M. R., & Gnedin, N. Y. 2011, ApJ, 729, 36
Laporte, N., Ellis, R. S., Boone, F., et al. 2017, ApJ, 837, L21
Le Floc'h, E., Aussel, H., Ilbert, O., et al. 2009, ApJ, 703, 222
Lewis, J. S. W., Ocvirk, P., Dubois, Y., et al. 2023, MNRAS, 519, 5987
Li, Q., Narayanan, D., & Davé, R. 2019, MNRAS, 490, 1425
Ma, X., Hopkins, P. F., Garrison-Kimmel, S., et al. 2018, MNRAS, 478, 1694
Madau, P., & Dickinson, M. 2014, ARA&A, 52, 415
Magnelli, B., Boogaard, L., Decarli, R., et al. 2020, ApJ, 892, 66
Mauerhofer, V., & Dayal, P. 2023, MNRAS, 526, 2196
McKinnon, R., Torrey, P., & Vogelsberger, M. 2016, MNRAS, 457, 3775
McLure, R. J., Dunlop, J. S., Cullen, F., et al. 2018, MNRAS, 476, 3991
Meurer, G. R., Heckman, T. M., & Calzetti, D. 1999, ApJ, 521, 64
Murphy, E. J., Condon, J. J., Schinnerer, E., et al. 2011, ApJ, 737, 67
Narayanan, D., Davé, R., Johnson, B. D., et al. 2018, MNRAS, 474, 1718
Narayanan, D., Turk, M. J., Robitaille, T., et al. 2021, ApJS, 252, 12
Nomoto, K., Tominaga, N., Umeda, H., Kobayashi, C., & Maeda, K. 2006, NuPhA, 777, 424
Oppenheimer, B. D., & Davé, R. 2006, MNRAS, 373, 1265
Pallottini, A., Ferrara, A., Gallerani, S., et al. 2022, MNRAS, 513, 5621
Paxton, B., Bildsten, L., Dotter, A., et al. 2011, ApJS, 192, 3
Paxton, B., Cantiello, M., Arras, P., et al. 2013, ApJS, 208, 4
Paxton, B., Marchant, P., Schwab, J., et al. 2015, ApJS, 220, 15
Péroux, C., & Howk, J. C. 2020, ARA&A, 58, 363
Pope, A., McKinney, J., Kamieneski, P., et al. 2023, ApJL, 951, L46
Pope, A., Montaña, A., Battisti, A., et al. 2017, ApJ, 838, 137
Rahmati, A., Pawlik, A. H., Raičević, M., & Schaye, J. 2013, MNRAS, 430, 2427
Robitaille, T. P. 2011, A&A, 536, A79
Salim, S., & Narayanan, D. 2020, ARA&A, 58, 529
Scalo, J., & Elmegreen, B. G. 2004, ARA&A, 42, 275
Shapley, A. E., Sanders, R. L., Salim, S., et al. 2022, ApJ, 926, 145
Shen, X., Vogelsberger, M., Nelson, D., et al. 2022, MNRAS, 510, 5560
Smith, B. D., Bryan, G. L., Glover, S. C. O., et al. 2017, MNRAS, 466, 2217
Speagle, J. S., Steinhardt, C. L., Capak, P. L., & Silverman, J. D. 2014, ApJS, 214, 15
Tacconi, L. J., Genzel, R., & Sternberg, A. 2020, ARA&A, 58, 157
Thompson, R., 2014 Astrophysics Source Code Library, Soft, ascl:1411.001
Turk, M. J., Smith, B. D., Oishi, J. S., et al. 2011, ApJS, 192, 9
Vazdekis, A., Coelho, P., Cassisi, S., et al. 2015, MNRAS, 449, 1177
Vazdekis, A., Sánchez-Blázquez, P., Falcón-Barroso, J., et al. 2010, MNRAS, 404, 1639
Veilleux, S., Cecil, G., & Bland-Hawthorn, J. 2005, ARA&A, 43, 769
Vijayan, A. P., Thomas, P. A., Lovell, C. C., et al. 2024, MNRAS, 527, 7337
Vogelsberger, M., Nelson, D., Pillepich, A., et al. 2020, MNRAS, 492, 5167
Weingartner, J. C., & Draine, B. T. 2001, ApJ, 548, 296
Whitaker, K. E., Franx, M., Leja, J., et al. 2014, ApJ, 795, 104
Whitaker, K. E., Narayanan, D., Williams, C. C., et al. 2021, ApJL, 922, L30
Whitaker, K. E., Pope, A., Cybulski, R., et al. 2017, ApJ, 850, 208
Williams, C. C., Alberts, S., Ji, Z., et al. 2024, ApJ, 968, 40
Zavala, J. A., Casey, C. M., Manning, S. M., et al. 2021, ApJ, 909, 165